

3D Surface Reconstruction via the Photometric Stereo Method

JC Vaught and Ty Dangerfield

Department of Mechanical Engineering, University of South Carolina

December 7, 2025

Abstract

We present an analytical and numerical validation of the photometric stereo method used in industrial applications for defect detection. This paper details six primary contributions toward a synthetic photometric pipeline: (1) eight unique surface geometries, (2) rigorous mathematical solutions for both numerical and analytical approaches, (3) detailed algorithmic explanations for each primary component of the pipeline, (4) experimental validation across eight shapes and sixteen light-source locations, (5) ablation studies on number of lights, noise robustness, and resolution impacts, and (6) a comparison of two alternative solver methods and their impact on results. Three-dimensional reconstruction depth errors range from 0.022 through 0.147, well within acceptable tolerances and demonstrating robust recovery. Angular errors of the normals reconstruction remain below 3.5° for smooth surfaces and 2° for polyhedral shapes.

Table 1: Individual Contributions

Contribution	Primary Contributor(s)
MATLAB implementation of complete program	Ty Dangerfield
Python implementation of complete program	JC Vaught
Photometric principle derivation	Ty Dangerfield & JC Vaught
Gradient integration with Poisson solver	Ty Dangerfield
Separation of variables and numerical derivations	JC Vaught
Report chapters 1, 3, and 4 (initial)	JC Vaught
Report chapters 1, 2, and 5 (initial)	Ty Dangerfield
Report restructuring and enhanced documentation	JC Vaught & Ty Dangerfield
Code architecture refinement and expansion	JC Vaught & Ty Dangerfield

Table 2: Meeting Participation

Date	JC Vaught	Ty Dangerfield
19 Nov 2025	Present	Present
20 Nov 2025	Present	Present
07 Dec 2025	Present	Present

Contents

1	Introduction	3
1.1	What We Want to Model	3
1.2	Why This Problem is Important	3
1.3	Comparison with Alternative Methods	4
1.4	The Core PDE Problem	4
2	Mathematical Foundation	5
2.1	Photometric Stereo Principle	5
2.1.1	Image Formation Model	5
2.1.2	Lambertian Reflectance	6
2.1.3	The Linear System Formulation	6
2.1.4	Least-Squares Solution via Pseudoinverse	7
2.1.5	Conditioning and Noise Sensitivity	8
2.1.6	Shadow Handling and Robust Estimation	8
2.2	Gradient Integration via Poisson Equation	9
2.2.1	Variational Formulation	9
2.2.2	Euler–Lagrange Derivation	9
2.3	Boundary Condition Theory	10
2.3.1	Dirichlet Boundary Conditions	10
2.3.2	Neumann Boundary Conditions	10
2.3.3	Periodic Boundary Conditions	10
2.3.4	Compatibility and Uniqueness	11
2.4	Analytical Solution via Separation of Variables	11
2.4.1	Eigenfunction Expansion	12
3	Numerical Methods	13
3.1	From Continuous PDE to Discrete Grid	13
3.1.1	Approximating Derivatives (Taylor Series)	13
3.1.2	The 5-Point Stencil Pattern	13
3.1.3	Building the Linear System	14
3.2	Solver 1: FFT-Based (Spectral Method)	15
3.2.1	Mathematical Approach	15
3.2.2	Boundary Condition: Periodic	16
3.2.3	Algorithm Steps	16

1 Introduction

1.1 What We Want to Model

Three-dimensional surface reconstruction is a fundamental problem in manufacturing applications and mechanical engineering more broadly. Photometric stereo is one possible solution among many, yielding highly accurate surface reconstruction compared to a dual-camera setup, which is more often used in robotic applications.

Given multiple 2D images of an object illuminated from different directions, we derive the PDE, analytical solution, and numerical solution that create an accurate reconstruction of the 3D depth map or surface geometry.

1.2 Why This Problem is Important

Photometric stereo has impact across multiple domains summarized in Table 3, including industrial inspection, where it supports surface defect detection and tolerance verification; medical imaging, where it enables high-fidelity reconstructions of anatomical surfaces for planning; archaeology, where non-destructive digitization preserves fragile artifacts; robotics and autonomous systems, where detailed surface geometry informs grasping and navigation; and reverse engineering, where recovered shapes seed CAD models for subsequent design and analysis.

Table 3: Representative Application Domains for Photometric Stereo

Domain	Example Use
Industrial inspection	Surface defect detection, geometric tolerance checks
Medical imaging	Preoperative surface reconstruction for planning
Archaeology	Non-destructive digitization of artifacts
Robotics	Shape-aware grasp planning and manipulation
Autonomous vehicles	High-fidelity surface maps for navigation
Reverse engineering	Recovering geometry for CAD modeling

Photometric stereo is an ideal solution for many surface extraction tasks owing to the reduction in moving parts. For example, in structure-from-motion methods, the movement of the camera must be precisely monitored and controlled, necessitating careful calibration; even minor calibration errors can severely impact reconstruction quality. Stereo cameras avoid motion but still suffer from calibration issues because the distance, angle, and focal length of each camera—the intrinsic parameters—must be known precisely to estimate depth. Any error there can distort the recovered geometry due to the trigonometric basis of the method. Photometric stereo, on the other hand, is a completely solid-state approach with a single camera, operates at a higher rate than structure-from-motion, and has lower data requirements than stereo systems. Because it leverages illumination direction to infer depth from shading and then reconstruct normals, it is inherently more tolerant to noise and avoids multi-camera calibration drift.

However, photometric stereo does suffer from one critical constraint: the illumination sequence must be precisely controlled. As a result, it cannot be used effectively in uncontrolled environments such as UAVs or general-purpose robotics, which is why stereo cameras remain the de facto standard outside manufacturing despite their calibration sensitivity. Nevertheless, the fundamental challenge in photometric stereo still lies in *integrating* noisy normal estimates into a globally consistent 3D surface, which requires solving a partial differential equation: the **Poisson equation**.

1.3 Comparison with Alternative Methods

Table 4 compares photometric stereo with other common 3D reconstruction techniques across key performance dimensions. The comparison highlights why photometric stereo is particularly well-suited for controlled industrial environments despite requiring specialized lighting infrastructure.

Table 4: Comparison of 3D Reconstruction Methods

Method	Advantages	Disadvantages	Typical Use Cases
Photometric Stereo	Single camera; high spatial resolution; dense surface normals; solid-state (no moving parts)	Requires controlled lighting; assumes Lambertian reflectance; limited to near-field	Defect detection, material inspection, quality control
Stereo Vision	Passive (no special lighting); works outdoors; real-time capable	Requires precise calibration; texture-dependent; ambiguity in textureless regions	Robotics, autonomous vehicles, SLAM
Structure from Motion	Single camera; scales to large scenes; robust to illumination changes	Requires camera motion; computationally intensive; drift accumulation	3D scanning, mapping, archaeological digitization
Structured Light	High accuracy; active illumination; fast acquisition	Sensitive to ambient light; limited range; projector-camera calibration required	Industrial metrology, 3D printing, facial scanning
Time-of-Flight	Direct depth measurement; real-time; works in low texture	Lower resolution; sensitive to multipath reflections; expensive hardware	Gesture recognition, indoor navigation, human-computer interaction

Photometric stereo excels in industrial settings where lighting can be tightly controlled and surface finish is relatively uniform. The method’s ability to capture dense normal fields from a single viewpoint makes it ideal for in-line inspection systems where throughput and repeatability are critical. By contrast, methods like stereo vision or time-of-flight are better suited to unstructured environments (e.g., outdoor robotics) where lighting variability and scene dynamics preclude the use of synchronized illumination sequences.

1.4 The Core PDE Problem

The fundamental problem reduces to solving the 2D Poisson equation in a rectangular domain:

$$\nabla^2 z(x, y) = f(x, y), \quad (x, y) \in \Omega = [0, L_x] \times [0, L_y] \quad (1)$$

where

$$\begin{aligned} z(x, y) &= \text{unknown surface height over the image domain} \\ f(x, y) &= \frac{\partial p}{\partial x} + \frac{\partial q}{\partial y} \quad (\text{divergence of Poisson-derived gradient estimates}) \\ \Omega &= [0, L_x] \times [0, L_y] \quad (\text{rectangular image domain}) \end{aligned}$$

This project demonstrates both analytical (separation of variables) and numerical (FFT-based and finite-difference) methods to solve this fundamental PDE and validate the solutions on synthetic 3D surfaces.

2 Mathematical Foundation

This chapter establishes the theoretical foundations for photometric stereo reconstruction. We begin with the photometric stereo principle, deriving the relationship between observed image intensities and surface normals under Lambertian reflectance. We then formulate the gradient integration problem as a Poisson equation, providing both variational and Euler-Lagrange derivations. Next, we develop the theory of boundary conditions—Dirichlet, Neumann, and periodic—and their impact on solution uniqueness. Finally, we present an analytical solution via separation of variables, including eigenfunction expansions and worked examples that validate our numerical methods.

2.1 Photometric Stereo Principle

Photometric stereo recovers surface normals from multiple images of a static scene illuminated by different light sources. The key insight is that shading variations across images encode the local surface orientation. Table 5 summarizes the key modeling assumptions underlying this approach.

Table 5: Photometric Stereo Modeling Assumptions

Assumption	Description
Lambertian reflectance	Surface reflects light diffusely in all directions; no specular highlights or glossy reflections
Orthographic projection	Camera uses parallel projection (unit focal length); no perspective distortion
Known light directions	Light source directions \mathbf{L}_i are calibrated and known a priori
Static scene	Surface geometry and camera remain fixed across all images
Uniform albedo	In our derivations, albedo $\rho(x, y)$ is assumed constant, though the general formulation allows spatially varying albedo
No inter-reflections	Light reaches the surface directly without bouncing off other surfaces
Attached shadows only	Self-shadowing is handled via the max operator; cast shadows from other objects are not modeled

2.1.1 Image Formation Model

By assuming an ideal camera with a unit focal length, we map a 3D point \mathbf{X} to image coordinates $\mathbf{x} = (x, y)$ for any arbitrary surface with depth $z(x, y)$. The measured image intensity I_i at pixel (x, y) under light source i is the product of three components: the camera calibration factor κ_i (encapsulating exposure, gain, and light source intensity), the material albedo $\rho(x, y) \in [0, 1]$ (the fraction of light reflected by the surface), and the geometric factor $\max(0, \mathbf{n}(x, y) \cdot \mathbf{L}_i)$ (the cosine of the angle between the surface normal \mathbf{n} and light direction \mathbf{L}_i). These combine to yield the image formation equation:

$$I_i(x, y) = \kappa_i \rho(x, y) \max(0, \mathbf{n}(x, y) \cdot \mathbf{L}_i) \quad (2)$$

The max operator enforces attached shadows: when a light illuminates the surface from behind ($\mathbf{n} \cdot \mathbf{L}_i < 0$), the contribution is zero.

2.1.2 Lambertian Reflectance

The Lambertian assumption states that a surface appears equally bright from all viewing directions—light is reflected diffusely in all directions. Mathematically, the reflected radiance is proportional to $\cos \theta = \mathbf{n} \cdot \mathbf{L}$, where θ is the angle between the surface normal and the incident light direction.

To connect surface geometry to shading, we must express the surface normal in terms of the depth map $z(x, y)$. We begin by computing the tangent vectors to the surface. These tangent vectors represent the local orientation of the surface along the x and y coordinate directions:

$$\frac{\partial \mathbf{X}}{\partial x} = (1, 0, p), \quad \text{where } p = \frac{\partial z}{\partial x} \quad (3)$$

$$\frac{\partial \mathbf{X}}{\partial y} = (0, 1, q), \quad \text{where } q = \frac{\partial z}{\partial y} \quad (4)$$

Here, p and q represent the local slopes of the surface in the x and y directions, respectively. Note that the first two components of each tangent vector are $(1, 0)$ and $(0, 1)$ because we move one unit along the respective image coordinate while the surface height changes by p or q .

The surface normal is perpendicular to both tangent vectors and can be computed via their cross product:

$$\tilde{\mathbf{n}} = \frac{\partial \mathbf{X}}{\partial x} \times \frac{\partial \mathbf{X}}{\partial y} = (-p, -q, 1) \quad (5)$$

This unnormalized normal $\tilde{\mathbf{n}}$ points away from the surface but does not necessarily have unit length. The negative signs on p and q arise naturally from the cross product and ensure the normal points outward (away from the surface) rather than inward.

To obtain a unit normal vector (required for computing the geometric factor $\mathbf{n} \cdot \mathbf{L}$), we divide by the magnitude:

$$\mathbf{n} = \frac{\tilde{\mathbf{n}}}{\|\tilde{\mathbf{n}}\|} = \frac{(-p, -q, 1)}{\sqrt{p^2 + q^2 + 1}} \quad (6)$$

Equation (6) explicitly links the integrable gradient field (p, q) to the observed shading—this is the key relationship that enables gradient recovery from images.

2.1.3 The Linear System Formulation

Having established the relationship between surface normals and image intensities, we now formulate the inverse problem: given multiple images under different illumination, recover the surface normal at each pixel.

We introduce the scaled normal vector $\mathbf{g}(x, y) = \rho(x, y)\mathbf{n}(x, y)$, which combines the geometric information (normal direction) with the material property (albedo). This factorization is convenient because \mathbf{g} appears linearly in the image formation equation.

Substituting the Lambertian reflectance model (6) into the image formation equation (2), we obtain for a single light source i :

$$I_i(x, y) = \kappa_i \mathbf{L}_i^T \mathbf{g}(x, y) \quad (7)$$

where we have absorbed the max operator into the formulation (assuming no self-shadowing for now; we address this later). This is a scalar equation linear in \mathbf{g} .

For m different light sources, we obtain m such equations at each pixel. Stacking these into a single matrix equation yields:

$$\underbrace{\begin{bmatrix} I_1(x, y) \\ I_2(x, y) \\ \vdots \\ I_m(x, y) \end{bmatrix}}_{\mathbf{I}(x, y) \in \mathbb{R}^m} = \underbrace{\begin{bmatrix} \kappa_1 \mathbf{L}_1^T \\ \kappa_2 \mathbf{L}_2^T \\ \vdots \\ \kappa_m \mathbf{L}_m^T \end{bmatrix}}_{S \in \mathbb{R}^{m \times 3}} \underbrace{\mathbf{g}(x, y)}_{\in \mathbb{R}^3} \quad (8)$$

Compactly, we write:

$$S\mathbf{g}(x, y) = \mathbf{I}(x, y) \quad (9)$$

The matrix S is called the *illumination matrix* and depends only on the known light directions and calibration factors. The vector $\mathbf{I}(x, y)$ contains the observed intensities, and our goal is to solve for $\mathbf{g}(x, y)$ at every pixel. For a unique solution to exist, S must have full column rank: $\text{rank}(S) = 3$. This requires at least three images ($m \geq 3$) with non-coplanar light directions. In practice, we use $m > 3$ to obtain an overdetermined system, which provides robustness against noise.

2.1.4 Least-Squares Solution via Pseudoinverse

When $m > 3$, the system (9) is overdetermined and generally has no exact solution due to measurement noise. We instead seek the least-squares solution that minimizes the residual:

$$\hat{\mathbf{g}}(x, y) = \arg \min_{\mathbf{g}} \|S\mathbf{g} - \mathbf{I}(x, y)\|_2^2 \quad (10)$$

Expanding the objective function:

$$\|S\mathbf{g} - \mathbf{I}\|_2^2 = (S\mathbf{g} - \mathbf{I})^T (S\mathbf{g} - \mathbf{I}) = \mathbf{g}^T S^T S \mathbf{g} - 2\mathbf{I}^T S \mathbf{g} + \mathbf{I}^T \mathbf{I} \quad (11)$$

Taking the gradient with respect to \mathbf{g} and setting it to zero yields the *normal equations*:

$$\nabla_{\mathbf{g}} \|S\mathbf{g} - \mathbf{I}\|_2^2 = 2S^T S \mathbf{g} - 2S^T \mathbf{I} = 0 \Rightarrow S^T S \mathbf{g} = S^T \mathbf{I} \quad (12)$$

Assuming S has full column rank, $S^T S$ is invertible, and we obtain:

$$\mathbf{g}(x, y) = \underbrace{(S^T S)^{-1} S^T}_{S^+ \text{ (pseudoinverse)}} \mathbf{I}(x, y) \quad (13)$$

The matrix $S^+ = (S^T S)^{-1} S^T$ is the Moore–Penrose pseudoinverse of S . This solution minimizes the L^2 norm of the residual and is unique when $\text{rank}(S) = 3$. Once $\mathbf{g}(x, y)$ is computed, we recover the unit normal and albedo by exploiting the factorization $\mathbf{g} = \rho \mathbf{n}$:

$$\hat{\rho}(x, y) = \|\mathbf{g}(x, y)\|_2 \quad (14)$$

$$\hat{\mathbf{n}}(x, y) = \frac{\mathbf{g}(x, y)}{\|\mathbf{g}(x, y)\|_2} \quad (15)$$

The *direction* of \mathbf{g} encodes the surface normal while its *magnitude* equals the albedo.

2.1.5 Conditioning and Noise Sensitivity

The accuracy of the recovered normals depends critically on the *condition number* of S :

$$\kappa(S) = \frac{\sigma_{\max}(S)}{\sigma_{\min}(S)} \quad (16)$$

where σ_{\max} and σ_{\min} are the largest and smallest singular values of S , respectively. To understand the impact of conditioning, consider the singular value decomposition (SVD) of S :

$$S = U\Sigma V^T \quad (17)$$

where $U \in \mathbb{R}^{m \times 3}$ and $V \in \mathbb{R}^{3 \times 3}$ are orthogonal matrices, and $\Sigma = \text{diag}(\sigma_1, \sigma_2, \sigma_3)$ contains the singular values in descending order. The pseudoinverse can be expressed as:

$$S^+ = V\Sigma^{-1}U^T \quad (18)$$

If the measured intensities contain noise $\Delta\mathbf{I}$ such that $\|\Delta\mathbf{I}\|/\|\mathbf{I}\| = \epsilon$, the relative error in the recovered \mathbf{g} is bounded by:

$$\frac{\|\Delta\mathbf{g}\|}{\|\mathbf{g}\|} \leq \kappa(S) \cdot \epsilon \quad (19)$$

This shows that the condition number $\kappa(S)$ controls the worst-case amplification of measurement noise. A large condition number indicates that small errors in \mathbf{I} can lead to large errors in \mathbf{g} . To minimize noise sensitivity, we seek to minimize $\kappa(S)$, or equivalently, maximize $\sigma_{\min}(S)$. This is achieved when the light directions $\{\mathbf{L}_i\}$ are uniformly distributed over the unit sphere, ensuring that the columns of S span \mathbb{R}^3 evenly. In practice, lights are often arranged in a hemispherical configuration with uniform azimuthal and elevation spacing. Using $m > 3$ images provides two additional benefits: the least-squares solution averages out random noise, and the system becomes more robust to individual measurements corrupted by saturation or outliers.

2.1.6 Shadow Handling and Robust Estimation

The linear system (9) assumes that all lights illuminate the surface from the front ($\mathbf{n} \cdot \mathbf{L}_i > 0$). When a light source illuminates from behind, *self-shadowing* occurs, and the image formation equation becomes:

$$I_i(x, y) = 0 \quad \text{if } \mathbf{n}(x, y) \cdot \mathbf{L}_i < 0 \quad (20)$$

These shadowed measurements violate the linear model and must be excluded. The standard approach is to first identify light sources i for which $I_i(x, y) \approx 0$ (or below a threshold), then remove the corresponding rows from S and entries from $\mathbf{I}(x, y)$, and finally solve the reduced least-squares problem on the remaining valid measurements. This row deletion strategy preserves the least-squares structure and ensures that only valid measurements contribute to the normal estimate. However, it requires at least three non-shadowed lights at every pixel to maintain $\text{rank}(S) = 3$.

For pixels near shadow boundaries where intensities are low but non-zero, a weighted least-squares approach provides a smoother alternative:

$$\hat{\mathbf{g}} = \arg \min_{\mathbf{g}} \sum_{i=1}^m w_i (I_i - \kappa_i \mathbf{L}_i^T \mathbf{g})^2 \quad (21)$$

where weights w_i are set based on confidence (e.g., $w_i = \max(0, \mathbf{n} \cdot \mathbf{L}_i)$ or based on intensity magnitude). This provides a smooth transition between fully illuminated and shadowed regions.

2.2 Gradient Integration via Poisson Equation

We now have the normals $\mathbf{g}(x, y)$ from photometric stereo, but our ultimate goal is a height map $z(x, y)$. The normals allow us to compute gradient estimates $(p, q) = (\partial z / \partial x, \partial z / \partial y)$, but real measurements are noisy and generally not integrable—the curl $\partial_y p - \partial_x q \neq 0$. This section develops the variational framework that projects noisy gradients onto the closest integrable field.

2.2.1 Variational Formulation

Given noisy gradient estimates (\hat{p}, \hat{q}) from photometric stereo, we seek a height field $z(x, y)$ whose gradients best match the measurements in a least-squares sense. This leads to the variational problem:

$$\min_z \mathcal{E}[z] = \iint_{\Omega} [(\partial_x z - \hat{p})^2 + (\partial_y z - \hat{q})^2] dx dy \quad (22)$$

The functional $\mathcal{E}[z]$ measures the total squared error between the true gradients $(\partial_x z, \partial_y z)$ of the unknown surface and the measured estimates (\hat{p}, \hat{q}) . By minimizing over all possible height functions z , we find the surface whose gradients are closest to the measurements in the L^2 norm.

The integrand $\mathcal{L} = (\partial_x z - \hat{p})^2 + (\partial_y z - \hat{q})^2$ depends on z only through its first derivatives $z_x = \partial_x z$ and $z_y = \partial_y z$. This structure is characteristic of problems in the calculus of variations, and the minimizer satisfies the Euler–Lagrange equation.

2.2.2 Euler–Lagrange Derivation

For a functional of the form $\mathcal{E}[z] = \iint \mathcal{L}(z, z_x, z_y) dx dy$, the necessary condition for a minimum is the Euler–Lagrange equation:

$$\frac{\partial \mathcal{L}}{\partial z} - \frac{\partial}{\partial x} \left(\frac{\partial \mathcal{L}}{\partial z_x} \right) - \frac{\partial}{\partial y} \left(\frac{\partial \mathcal{L}}{\partial z_y} \right) = 0 \quad (23)$$

Since our Lagrangian $\mathcal{L} = (z_x - \hat{p})^2 + (z_y - \hat{q})^2$ does not depend on z directly, we have $\partial \mathcal{L} / \partial z = 0$. Computing the remaining partial derivatives:

$$\frac{\partial \mathcal{L}}{\partial z_x} = 2(z_x - \hat{p}), \quad \frac{\partial \mathcal{L}}{\partial z_y} = 2(z_y - \hat{q}) \quad (24)$$

Substituting into the Euler–Lagrange equation:

$$\frac{\partial}{\partial x} [2(z_x - \hat{p})] + \frac{\partial}{\partial y} [2(z_y - \hat{q})] = 0 \quad (25)$$

Expanding and rearranging:

$$\partial_x^2 z + \partial_y^2 z = \partial_x \hat{p} + \partial_y \hat{q} \quad (26)$$

This is the Poisson equation:

$$\nabla^2 z = f(x, y), \quad \text{where } f = \nabla \cdot (\hat{p}, \hat{q}) = \frac{\partial \hat{p}}{\partial x} + \frac{\partial \hat{q}}{\partial y} \quad (27)$$

Here $\nabla^2 = \partial_x^2 + \partial_y^2$ is the Laplacian operator and $f(x, y)$ is the divergence of the measured gradient field. The Poisson equation (27) arises because an integrable vector field must be curl-free ($\partial_y \hat{p} - \partial_x \hat{q} = 0$). When the measured gradients violate this condition due to noise, solving the Poisson problem projects (\hat{p}, \hat{q}) onto the closest integrable field in the L^2 sense.

2.3 Boundary Condition Theory

The Poisson equation $\nabla^2 z = f$ admits a unique solution only when supplemented with boundary conditions on $\partial\Omega$. We consider three types that arise in surface reconstruction: Dirichlet, Neumann, and periodic conditions. The choice of boundary conditions depends on the physical assumptions about the surface at the image boundary and impacts both solution uniqueness and numerical implementation.

2.3.1 Dirichlet Boundary Conditions

Dirichlet conditions prescribe the solution value on the boundary:

$$z(x, y) = g(x, y), \quad (x, y) \in \partial\Omega \quad (28)$$

where g is a given function. In the homogeneous case $g \equiv 0$, the surface is pinned to zero height along the entire boundary. This is appropriate when the reconstructed object is known to be flat at the image edges or when the object of interest is contained entirely within the interior of the domain.

For photometric stereo, homogeneous Dirichlet conditions assume that the surface height is zero (or a known constant) at the image boundary. This is suitable for objects that sit on a flat background plane or when the region of interest is masked to exclude edge artifacts. Dirichlet problems always have a unique solution given smooth data.

2.3.2 Neumann Boundary Conditions

Neumann conditions prescribe the normal derivative at the boundary:

$$\left. \frac{\partial z}{\partial n} \right|_{\partial\Omega} = h(x, y), \quad (x, y) \in \partial\Omega \quad (29)$$

where \mathbf{n} is the outward unit normal to $\partial\Omega$ and h specifies the boundary flux. The homogeneous case $h \equiv 0$ imposes zero normal derivative, meaning the surface approaches the boundary with zero slope in the perpendicular direction.

Zero-flux Neumann conditions arise when we have no information about the surface beyond the image boundary. The natural continuation of the gradient field is to assume it stays flat, preventing artificial discontinuities. However, Neumann conditions leave the solution determined only up to an additive constant—we can recover the surface shape but not its absolute height. This lack of absolute height information is resolved by simply setting the average of the entire reconstructed depth profile to zero.

2.3.3 Periodic Boundary Conditions

Periodic conditions impose that the solution and its derivatives wrap around at opposite boundaries:

$$z(0, y) = z(L_x, y), \quad z(x, 0) = z(x, L_y), \quad \text{and similarly for derivatives} \quad (30)$$

This condition arises naturally when using Fourier-based (FFT) solvers, which assume the domain tiles infinitely in all directions. Under periodicity, the Discrete Fourier Transform diagonalizes the Laplacian operator, enabling $\mathcal{O}(N \log N)$ solution complexity.

Periodic conditions are rarely physical for real surfaces but are computationally convenient. They work well when the surface gradients decay to zero near the boundary (e.g., smooth objects

centered in the image) but can introduce artifacts when the surface value or gradient differs significantly between opposite edges. In practice, we often accept these artifacts in exchange for FFT solver speed, especially when the object of interest is well-separated from the image boundary.

2.3.4 Compatibility and Uniqueness

The three boundary condition types have different uniqueness and compatibility properties, which determine when a solution exists and whether it is unique up to an additive constant.

Dirichlet conditions guarantee a unique solution for any smooth right-hand side f and boundary data g . No additional constraints are required—the boundary values fully determine the solution.

Neumann conditions require a compatibility constraint. Applying the divergence theorem to the Poisson equation:

$$\iint_{\Omega} \nabla^2 z \, dA = \oint_{\partial\Omega} \frac{\partial z}{\partial n} \, ds \quad (31)$$

Substituting $\nabla^2 z = f$ and the Neumann condition $\partial z / \partial n = h$:

$$\iint_{\Omega} f \, dA = \oint_{\partial\Omega} h \, ds \quad (32)$$

For homogeneous Neumann conditions ($h = 0$), solvability requires:

$$\iint_{\Omega} f \, dA = 0 \quad (33)$$

In other words, the source term must integrate to zero over the domain. Even when this condition is satisfied, the solution is unique only up to an additive constant—any $z + c$ is also a solution. We select the unique solution with zero mean.

Periodic conditions have the same compatibility requirement as homogeneous Neumann. Since the domain wraps around with no boundary flux, the integral constraint $\iint f \, dA = 0$ must hold. In the FFT formulation, this corresponds to the DC component $\hat{F}[0, 0] = 0$ —the zero-frequency Fourier coefficient must vanish. The FFT solver enforces this by setting $\hat{F}[0, 0] = 0$ before division by the eigenvalues. Like Neumann, periodic conditions also leave an additive constant ambiguity, resolved by zero-mean normalization.

2.4 Analytical Solution via Separation of Variables

Before developing numerical integration schemes to solve the Poisson equation for our photometric stereo application, we first derive an analytical solution as a baseline for comparison—and, candidly, as an exercise to demonstrate mathematical rigor in the realm of partial differential equations.

The method of separation of variables yields closed-form expressions for problems with homogeneous boundary conditions on rectangular domains. By expanding the solution as a sum of orthogonal eigenfunctions, we obtain exact modal coefficients that serve as ground truth for validating numerical implementations. This section provides the theoretical foundation but will not be directly referenced in subsequent chapters; nevertheless, the analytical benchmark remains essential for verifying solver correctness during development.

2.4.1 Eigenfunction Expansion

Consider the 2D Poisson equation on a rectangular domain $\Omega = [0, L_x] \times [0, L_y]$ with homogeneous Dirichlet boundary conditions:

$$\nabla^2 z = f(x, y), \quad (x, y) \in \Omega, \quad z|_{\partial\Omega} = 0 \quad (34)$$

Using separation of variables, we assume $z(x, y) = X(x)Y(y)$. The homogeneous boundary conditions require $X(0) = X(L_x) = 0$ and $Y(0) = Y(L_y) = 0$, which are satisfied by sine functions. The solution can be written as an eigenfunction expansion:

$$z(x, y) = \sum_{m=1}^{\infty} \sum_{n=1}^{\infty} A_{mn} \sin\left(\frac{m\pi x}{L_x}\right) \sin\left(\frac{n\pi y}{L_y}\right) \quad (35)$$

Figure 1 illustrates how higher modes introduce additional oscillations. In one dimension, $\sin(m\pi x/L)$ has m half-cycles across the domain, so higher m values correspond to finer spatial detail.

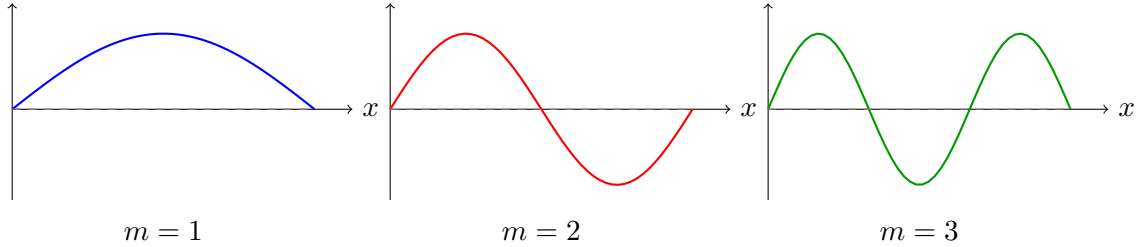


Figure 1: Eigenfunctions $\sin(m\pi x/L)$ for $m = 1, 2, 3$. The 2D eigenfunctions are products: $\sin(m\pi x/L_x) \sin(n\pi y/L_y)$. Higher modes oscillate more rapidly and contribute less to the solution because their eigenvalues $\lambda_{mn} \propto m^2 + n^2$ appear in the denominator.

The eigenfunctions form an orthonormal basis for the solution space. Each eigenfunction satisfies the Laplacian eigenvalue problem with eigenvalue $-\lambda_{mn}$ where:

$$\lambda_{mn} = \frac{m^2\pi^2}{L_x^2} + \frac{n^2\pi^2}{L_y^2} \quad (36)$$

Substituting the expansion into the Poisson equation and projecting onto each eigenfunction yields the modal amplitudes:

$$A_{mn} = -\frac{F_{mn}}{\lambda_{mn}}, \quad \text{where } F_{mn} = \frac{4}{L_x L_y} \int_0^{L_x} \int_0^{L_y} f(x, y) \sin\left(\frac{m\pi x}{L_x}\right) \sin\left(\frac{n\pi y}{L_y}\right) dy dx \quad (37)$$

The coefficient F_{mn} is the projection of the source term f onto each eigenfunction. This is precisely what FFT-based solvers compute numerically: the Discrete Fourier Transform projects the discretized f onto sinusoidal basis functions, and division by the eigenvalues λ_{mn} yields the solution coefficients.

3 Numerical Methods

Having established the mathematical framework for photometric stereo and gradient integration, we now turn to the numerical methods that enable practical computation. This chapter presents the techniques for converting the continuous Poisson equation into discrete systems that computers can solve efficiently.

We begin with the fundamental discretization approach—converting continuous derivatives to finite differences on a grid. This lays the groundwork for understanding all subsequent solvers. We then present three distinct Poisson solvers, each with different boundary condition assumptions and computational trade-offs. Finally, we address regularization techniques for handling noisy real-world data.

3.1 From Continuous PDE to Discrete Grid

The continuous Poisson equation $\nabla^2 z = f$ cannot be solved directly by computers, which operate on discrete values. The finite difference method replaces continuous derivatives with algebraic approximations computed on a regular grid of sample points. This section derives these approximations and shows how they lead to a large linear system.

3.1.1 Approximating Derivatives (Taylor Series)

Consider a function $z(x)$ sampled on a uniform grid with spacing h . To approximate derivatives, we use Taylor series expansions about a point x :

$$z(x+h) = z(x) + hz'(x) + \frac{h^2}{2}z''(x) + \frac{h^3}{6}z'''(x) + \mathcal{O}(h^4) \quad (38)$$

$$z(x-h) = z(x) - hz'(x) + \frac{h^2}{2}z''(x) - \frac{h^3}{6}z'''(x) + \mathcal{O}(h^4) \quad (39)$$

Adding these two equations eliminates the odd-order terms:

$$z(x+h) + z(x-h) = 2z(x) + h^2z''(x) + \mathcal{O}(h^4) \quad (40)$$

Solving for the second derivative yields the central difference formula:

$$z''(x) = \frac{z(x+h) - 2z(x) + z(x-h)}{h^2} + \mathcal{O}(h^2) \quad (41)$$

This approximation is second-order accurate—the error decreases quadratically as the grid spacing h is refined. On a discrete grid where $z_i = z(x_i)$, we write this as:

$$z''_i \approx \frac{z_{i+1} - 2z_i + z_{i-1}}{h^2} \quad (42)$$

3.1.2 The 5-Point Stencil Pattern

In two dimensions, the Laplacian combines second derivatives in both coordinate directions, capturing how the function curves in the x - and y -directions:

$$\nabla^2 z = \frac{\partial^2 z}{\partial x^2} + \frac{\partial^2 z}{\partial y^2} \quad (43)$$

Applying the central difference formula (41) in both directions at grid point (i, j) :

$$\nabla^2 z \Big|_{i,j} \approx \frac{z_{i+1,j} - 2z_{i,j} + z_{i-1,j}}{(\Delta x)^2} + \frac{z_{i,j+1} - 2z_{i,j} + z_{i,j-1}}{(\Delta y)^2} \quad (44)$$

For uniform spacing $h = \Delta x = \Delta y$, this simplifies to the 5-point stencil:

$$\boxed{\nabla^2 z \Big|_{i,j} \approx \frac{z_{i+1,j} + z_{i-1,j} + z_{i,j+1} + z_{i,j-1} - 4z_{i,j}}{h^2}} \quad (45)$$

The stencil pattern represents a local finite difference operator that combines values from the center point and its four nearest neighbors on the grid. Figure 2 visualizes the coefficient structure:

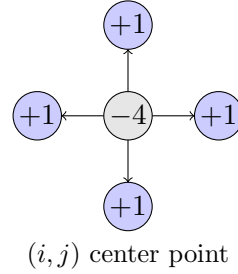


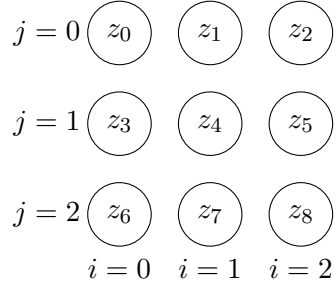
Figure 2: The 5-point Laplacian stencil weights.

The stencil computes a weighted average of the four neighbors minus four times the center value, all divided by h^2 . This approximates how the curvature (Laplacian) at a point relates to its deviation from the average of its neighbors.

3.1.3 Building the Linear System

To solve the Poisson equation numerically, we must convert the stencil operations into a single large linear system $A\mathbf{z} = \mathbf{f}$. This requires mapping the 2D grid to a 1D vector and translating neighbor relationships into matrix entries.

Consider a simple 3×3 grid with 9 unknowns. Using row-major ordering, we assign linear index $k = i + j \cdot W$ where $W = 3$ is the grid width:



For an interior point like z_4 (at position $i = 1, j = 1$), the 5-point stencil couples it to its four neighbors:

$$\frac{z_5 + z_3 + z_7 + z_1 - 4z_4}{h^2} = f_4 \quad (46)$$

This becomes one row of the linear system. Rearranging with unknowns on the left:

$$\frac{1}{h^2}z_1 + \frac{1}{h^2}z_3 - \frac{4}{h^2}z_4 + \frac{1}{h^2}z_5 + \frac{1}{h^2}z_7 = f_4 \quad (47)$$

Writing this for all 9 grid points simultaneously yields the matrix equation $A\mathbf{z} = \mathbf{f}$. The matrix A has a characteristic block structure:

$$A = \frac{1}{h^2} \begin{bmatrix} -4 & 1 & 0 & 1 & 0 & 0 & 0 & 0 & 0 \\ 1 & -4 & 1 & 0 & 1 & 0 & 0 & 0 & 0 \\ 0 & 1 & -4 & 0 & 0 & 1 & 0 & 0 & 0 \\ 1 & 0 & 0 & -4 & 1 & 0 & 1 & 0 & 0 \\ 0 & 1 & 0 & 1 & -4 & 1 & 0 & 1 & 0 \\ 0 & 0 & 1 & 0 & 1 & -4 & 0 & 0 & 1 \\ 0 & 0 & 0 & 1 & 0 & 0 & -4 & 1 & 0 \\ 0 & 0 & 0 & 0 & 1 & 0 & 1 & -4 & 1 \\ 0 & 0 & 0 & 0 & 0 & 1 & 0 & 1 & -4 \end{bmatrix} \quad (48)$$

Each row corresponds to one grid point. The diagonal entry is -4 (center weight), entries at ± 1 positions connect horizontal neighbors (same row), and entries at $\pm W$ positions connect vertical neighbors (adjacent rows). The matrix is sparse—only 5 entries per row instead of N —which is crucial for efficiency on large grids.

Boundary conditions modify the right-hand side \mathbf{f} or the matrix structure itself. For Dirichlet conditions, known boundary values move to the right-hand side. For Neumann conditions, stencil weights at boundaries are adjusted to enforce derivative constraints. The specific modifications are detailed in the solver sections that follow.

3.2 Solver 1: FFT-Based (Spectral Method)

The FFT-based solver exploits the fact that the Laplacian operator is diagonalized in the Fourier domain. This transforms the Poisson PDE into simple algebraic division, enabling $\mathcal{O}(N \log N)$ solution complexity. This is our fastest solver and the default choice when periodic boundary conditions are acceptable.

3.2.1 Mathematical Approach

The key insight is that Fourier basis functions (complex exponentials) are eigenfunctions of the Laplacian. Applying the Fourier transform to both sides of $\nabla^2 z = f$:

$$\mathcal{F}\{\nabla^2 z\} = \mathcal{F}\{f\} \quad (49)$$

The Laplacian in the frequency domain becomes multiplication by eigenvalues. Let $\hat{Z}(\mathbf{k})$ and $\hat{F}(\mathbf{k})$ denote the Fourier transforms of z and f at frequency $\mathbf{k} = (k_x, k_y)$:

$$-|\mathbf{k}|^2 \hat{Z}(\mathbf{k}) = \hat{F}(\mathbf{k}) \quad (50)$$

where $|\mathbf{k}|^2 = k_x^2 + k_y^2$ is the squared frequency magnitude. Solving for the solution in frequency space:

$$\hat{Z}(\mathbf{k}) = \frac{\hat{F}(\mathbf{k})}{-|\mathbf{k}|^2} \quad (51)$$

The solution is obtained by inverse Fourier transform:

$$z(x, y) = \mathcal{F}^{-1} \left\{ \frac{\hat{F}(\mathbf{k})}{-\|\mathbf{k}\|^2} \right\} \quad (52)$$

This converts the PDE (which requires solving a large linear system) into three simple operations: forward FFT, element-wise division, and inverse FFT.

3.2.2 Boundary Condition: Periodic

The FFT inherently assumes that the signal is periodic in all directions. This means the solver implicitly enforces:

$$z(0, y) = z(L_x, y), \quad z(x, 0) = z(x, L_y), \quad \text{and similarly for all derivatives} \quad (53)$$

Periodic boundary conditions are rarely physical for real surfaces—few objects wrap around seamlessly at their edges. However, they work well when the object of interest is centered in the image with gradients decaying to near-zero at the boundaries.

A critical issue arises at the DC component ($\mathbf{k} = (0, 0)$): the eigenvalue $|\mathbf{k}|^2 = 0$, creating a division by zero. This corresponds to the compatibility condition from Section 2.3—periodic problems determine the solution only up to an additive constant. We handle this by setting $\hat{F}[0, 0] = 0$ to enforce zero-mean source (compatibility), setting the eigenvalue $\lambda[0, 0] = 1$ to avoid division by zero, and the resulting $\hat{Z}[0, 0] = 0$ gives a zero-mean solution.

3.2.3 Algorithm Steps

The complete FFT solver procedure is shown in Algorithm 1. The algorithm requires only two FFT operations (steps 2 and 6), each with $\mathcal{O}(N \log N)$ complexity, making this solver extremely fast for typical image sizes.

Algorithm 1 FFT-Based Poisson Solver

Require: Gradient estimates (p, q) from photometric stereo

Ensure: Height field z

- 1: Compute divergence: $f \leftarrow \partial_x p + \partial_y q$
 - 2: $\hat{F} \leftarrow \text{FFT2D}(f)$
 - 3: Construct eigenvalues: $\lambda_{k_x, k_y} \leftarrow -4\pi^2(k_x^2/L_x^2 + k_y^2/L_y^2)$
 - 4: Handle DC component: $\lambda[0, 0] \leftarrow 1$; $\hat{F}[0, 0] \leftarrow 0$
 - 5: $\hat{Z} \leftarrow \hat{F}/\lambda$
 - 6: $z \leftarrow \text{IFFT2D}(\hat{Z})$
 - 7: $z \leftarrow \text{Re}(z)$
 - 8: **return** z
-